Comparative Raman study of Ruddlesden-Popper nickelates and the monolayer-trilayer polymorph

Vignesh Sundaramurthy,[1] Abhi Suthar,[1] Pascal Puphal,[1] Congcong Le,[2] Yuhao Gu,[3] Hasan Yilmaz,[1,4] Pablo Sosa-Lizama,[1] Peter A. van Aken,[1] Y. Eren Suyolcu,[1] Masahiko Isobe,[1] Andreas P. Schnyder,[1] Xianxin Wu,[5] Matteo Minola,[1] Bernhard Keimer,[1] and Matthias Hepting[1,*]

[1]*Max-Planck-Institute for Solid State Research, Heisenbergstraße 1, 70569 Stuttgart, Germany*
[2]*Hefei National Laboratory, Hefei 230088, China*
[3]*School of Mathematics and Physics, University of Science and Technology Beijing, Beijing 100083, China*
[4]*University of Stuttgart, Institute for Materials Science, Materials Synthesis Group, Heisenbergstraße 3, 70569 Stuttgart, Germany*
[5]*Institute of Theoretical Physics, Chinese Academy of Sciences, Beijing 100190, China*

(Received 19 February 2026; revised 13 August 2026; accepted 20 October 2026; published 6 November 2026)

Ruddlesden-Popper (RP) nickelates have attracted intense interest following the discovery of superconductivity in several members of the series, including bilayer (BL) $La_3Ni_2O_7$, trilayer (TL) $La_4Ni_3O_{10}$, and structural polymorphs composed of monolayer-bilayer or monolayer-trilayer (ML-TL) units. However, an inherent propensity of the RP series to form intergrown phases during single-crystal synthesis, together with spatial variations in oxygen stoichiometry, has complicated the determination of their intrinsic material properties. As a consequence, conflicting reports have emerged on both their electronic phase transitions and lattice dynamics. In this work, we perform a comparative study of the phononic and electronic Raman responses of high-quality ML-TL single crystals and contrast them with those of the other RP nickelates, using samples with optimized oxygen content. We establish several Raman spectral features that enable unambiguous phase identification across the series. Moreover, we uncover characteristics in the phononic and electronic Raman response of ML-TL that are not reflected in the pure ML and TL compounds. We attribute these differences to a distinctive electronic structure arising from self-doping and confinement effects induced by the ML unit within the ML-TL lattice architecture.

DOI: 10.1103/m2js-yzky

I. INTRODUCTION

The search for high-T_c unconventional superconductivity beyond the layered cuprates has long been guided by the idea that materials sharing key structural and electronic configurations with cuprates might host similar physics [1]. Shortly after the discovery of superconductivity in hole-doped cuprates, nickelates with composition RE_2NiO_4 (RE = rare-earth ion) were intensively investigated as natural candidates [2]. This interest was motivated by the chemical proximity of Ni and Cu and by the observation of charge and spin stripe order [3], reminiscent of the stripe phases in hole-doped La_2CuO_4 [4], where they precede the onset of superconductivity [5,6]. Despite extensive experimental and theoretical efforts, however, superconductivity has never been conclusively established in nickelates composed of single layers of NiO_6 octahedra [7], such as hole-doped $RE_{2-x}Sr_xNiO_4$ [8]. Superconductivity has likewise not been observed in nickelate heterostructures with ultrathin perovskite layers [9] that were predicted to realize a cupratelike electronic structure [10,11].

A critical advance came with the discovery of superconductivity in thin films of hole-doped infinite-layer (IL) nickelates [12–14]. These materials exhibit square-planar NiO_2 layers without apical oxygen stacked along the c-axis direction, a structural motif that had been predicted by early theoretical work to be favorable for cupratelike electronic states [15]. Subsequent extensions to related IL-derived systems, including the quintuple-layer compound $Nd_6Ni_5O_{12}$ [16], demonstrated that superconductivity is not restricted to a unique structural realization, but might instead emerge across a broader nickelate materials space. Indeed, superconductivity was subsequently observed in single crystals of the bilayer (BL) nickelate $La_3Ni_2O_7$, which contains apical oxygen, with transition temperatures exceeding 80 K under high pressure [17]. Superconductivity was also reported in epitaxial thin films of the same compound, without the need for external pressure application [18,19]. The remarkably high T_c in BL single crystals surpasses the boiling point of liquid nitrogen and therefore represents a major milestone in the search for new families of high-T_c superconductors [20].

Both the BL compound and the earlier investigated monolayer (ML) nickelates belong to the Ruddlesden-Popper (RP) series [21], described by the empirical formula $RE_{n+1}Ni_nO_{3n+1}$, which consists of n perovskitelike NiO_6 layers separated by rock-salt REO blocks. Following the BL compound, superconductivity was also reported in the trilayer

*Contact author: hepting@fkf.mpg.de

Published by the American Physical Society under the terms of the Creative Commons Attribution 4.0 International license. Further distribution of this work must maintain attribution to the author(s) and the published article's title, journal citation, and DOI. Open access publication funded by Max Planck Society.

(TL) nickelate $La_4Ni_3O_{10}$, albeit with a lower T_c of 30 to 40 K [22,23]. This trend contrasts with the layer dependence observed in cuprates, where T_c typically increases from single-layer to multilayer systems [5,24], and points to a distinct and nontrivial interplay between crystal structure and electronic properties in RP nickelates [22,23,25–30].

Nonetheless, the superconducting phases of BL and TL nickelates emerge in close proximity to charge density wave (CDW) and spin density wave (SDW) instabilities, reminiscent of the behavior observed in cuprate and iron-based superconductors [5,6,31]. In TL nickelates, intertwined CDW and SDW order condense below approximately 140 K [32], whereas in BL nickelates the two orders are disjoint, with $T_{SDW} \approx 150$ K and $T_{CDW} \approx 110$ K [33]. These density-wave (DW) instabilities have been investigated using a variety of spectroscopic techniques, including angle-resolved photoemission spectroscopy (ARPES), muon spin rotation/relaxation (μSR), and Raman scattering [34–46]. Specifically, recent polarized Raman measurements have revealed a multiorbital character of the DW instability, involving both Ni $3d_{x^2-y^2}$ and $3d_{z^2}$ states [47].

Beyond the conventional RP phases with uniform stacking of NiO_6 octahedral units, a tendency to form unconventional polymorphic structures during bulk single-crystal growth has been reported, yielding variants with alternating monolayer-bilayer (ML-BL) [48,49] or monolayer-trilayer (ML-TL) stacking sequences [50–52]. These materials are also referred to as the "1212" and "1313" phases, respectively. The ML-BL variant exhibits a T_c of approximately 60 K [49], whereas for the ML-TL polymorph reported T_c values range between 4 and 80 K [50,53]. Whether specific polymorphic arrangements of RP building blocks favor or suppress DW correlations, or support a decoupling of spin and charge degrees of freedom, remains under debate as the reported trends vary substantially and are likely influenced by differences in oxygen stoichiometry among samples [48–54]. Nevertheless, these polymorphs offer an additional avenue for probing the layer dependence of correlated electron phenomena in nickelates. At the same time, they introduce an added level of complexity beyond the already multiband and multiorbital nature of conventional RP nickelates [25,55–58], since multiple structural building blocks contribute simultaneously to their low-energy electronic structure.

In particular, ARPES measurements on the ML-TL polymorph revealed the presence of the additional ε pocket at the Fermi surface, exhibiting Ni $3d_{z^2}$ orbital character [59], which is absent in pure ML, BL, and TL phases [34,60,61]. Furthermore, the quantum confinement of the TL between the ML blocks along with possible charge transfer was proposed to alter correlation strength and Ni valences [62–66], possibly giving rise to distinct Fermi surface features, such as Fermi arcs [67]. It therefore remains an open and central question how these emergent electronic features in the polymorphs influence the DW instabilities and superconductivity, and more broadly how lattice degrees of freedom are intertwined with the low-energy electronic structure.

In this work, we use polarized Raman scattering to investigate the phononic and electronic Raman response of the ML-TL polymorph, in direct comparison to the Raman response of other relevant members of the RP nickelate series. We observe unique Raman spectral features for each material, serving as a spectral fingerprint to identify the phase. Notably, the TL phase and the ML-TL polymorph exhibit a strikingly similar phonon spectrum at room temperature, although with subtle distinctions. At lower temperatures, dramatically different spectral features unique to each structural motif emerge, demonstrating the significance of Raman spectroscopy in the study of polymorph structures. In electronic Raman scattering, we observe emergent features attributable to DW formation, with both distinctions and similarities compared to those reported for the pure BL and TL compounds.

II. MATERIALS AND METHODS

Single crystals of the RP series $La_{n+1}Ni_nO_{3n+1}$ were grown using a high-pressure high-temperature optical floating-zone (OFZ) furnace (Model HKZ, SciDre GmbH, Dresden). Details about sample synthesis and characterization are provided in the Supplemental Material [68].

The Raman spectra were obtained with a HORIBA Jobin Yvon LabRAM HR800 spectrometer in backscattering geometry, using a He-Ne laser (wavelength 632.8 nm) focused on the sample with a x50 magnification ultralong working distance objective. The laser power on the sample was less than 1 mW. The indicated temperatures were determined by Stokes/anti-Stokes intensity analysis. All plotted Raman spectra were divided by the Bose-Einstein factor. For low-temperature measurements, a Konti Micro helium-flow cryostat from CRYOVAC was used.

Phonon frequency calculations were performed using density functional theory (DFT) as implemented in the Vienna *Ab-initio* Simulation Package (VASP) code [69]. The Perdew-Burke-Ernzerhof (PBE) [70] exchange-correlation functional and the projector-augmented-wave (PAW) [71] approach were used. Lattice constants and internal atomic positions were relaxed using generalized gradient approximation (GGA), with a plane-wave cutoff energy of 600 eV. Forces were minimized to less than 0.001 eV/Å in the relaxation. The calculations were performed for the tetragonal $P4/mmm$ (No. 123) unit cell. This symmetry is adopted by the ML-TL polymorph under pressure [50] when the octahedral tilts characterizing the larger $Fmmm$ unit cell vanish. The relaxed structural parameters were $a, b = 3.84$ Å and $c = 20.24$ Å, obtained from the $P4/mmm$ structure under 1.5 GPa. In the phonon calculations, the cutoff energy was set to 400 eV for expanding the wave functions into plane-wave basis, and the number of k points was set to $3 \times 4 \times 4$ for a $1 \times 2 \times 2$ supercell. The real-space force constants of the supercells were calculated using density-functional perturbation theory (DFPT) [72] and the phonon frequencies were calculated from the force constants using the PHONOPY code [73,74].

III. RESULTS

A. Phase identification

Figures 1(a)–1(c) provide an overview of the lattice architectures of the ML La_2NiO_4, BL $La_3Ni_2O_7$, and TL $La_4Ni_3O_{10}$ RP nickelates, along with the ML-TL $La_3Ni_2O_7$ polymorph in Fig. 1(d). A wide-area survey using high-angle annular dark-field (HAADF) scanning transmission electron

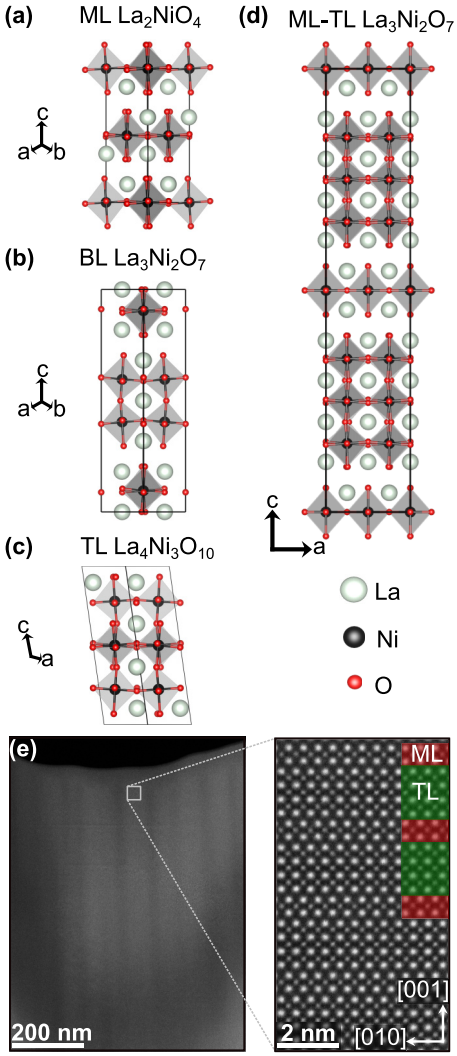


FIG. 1. (a)–(d) Schematics of the crystal structures of (a) ML La_2NiO_4, (b) BL $La_3Ni_2O_7$, (c) TL $La_4Ni_3O_{10}$, and (d) ML-TL $La_3Ni_2O_7$, with *Bmab*, *Amam*, $P2_1/a$, and *Fmmm* unit cells, respectively. (e) STEM-HAADF images of a ML-TL single crystal. The low-resolution image (left) demonstrates the absence of secondary phases on large length scales. The contrast between bright and dark vertical stripes corresponds to minor topographic differences due to curtaining effects caused by ion milling during specimen preparation. The atomic-resolution image (right) resolves the stacking sequence of ML (red) and TL (green) units. The [001] and [010] directions of the *Fmmm* unit cell are indicated.

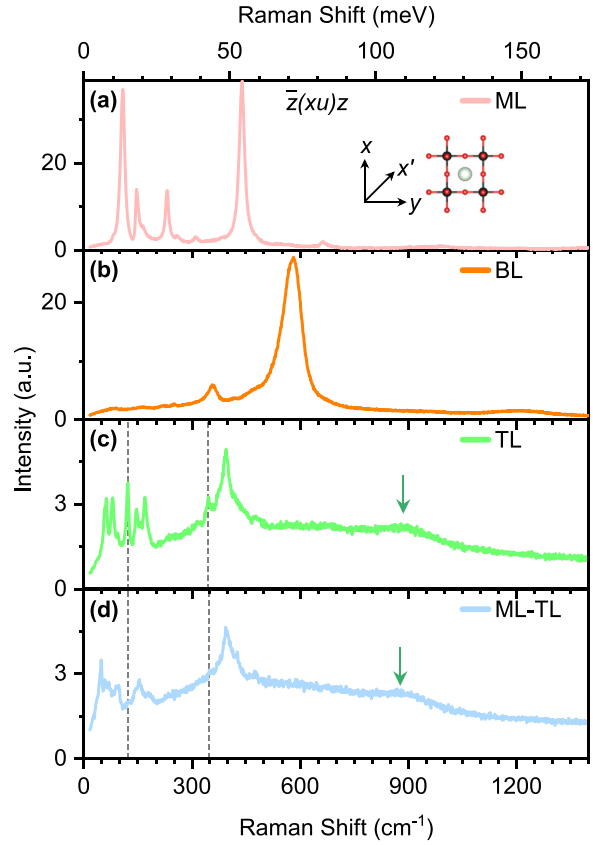


FIG. 2. (a)–(d) Raman spectra of the (a) ML, (b) BL, (c) TL, and (d) ML-TL phases acquired at room temperature in $\bar{z}(xu)z$ scattering configuration (without analyzer). The inset in (a) shows the top view of a Ni-O plaquette in the *ab* plane of layered nickelates, with octahedral tilts omitted for simplicity. The x and y directions of the laboratory frame of the Raman experiment point along the Ni-O-Ni bond directions. The x' direction is also indicated. Vertical dashed lines in (c) and (d) indicate the position of characteristic phonon modes of the TL phase that are absent in ML-TL. Green arrows mark a broad electronic Raman feature present in both TL and ML-TL.

microscopy (STEM) on an ML-TL single crystal used for the Raman measurements demonstrates high crystalline quality and the absence of secondary phases on macroscopic length scales (Fig. 1(e), left panel). Atomic-resolution HAADF imaging from a representative area resolves the characteristic alternating stacking of ML and TL structural units (Fig. 1(e), right panel). Note that phase-pure ML-TL single crystals grown by the OFZ technique reach lateral dimensions of several tens to a few hundred micrometers [50,51,54], whereas larger crystals typically contain mixed-phase regions. The spatial resolution of micro-Raman spectroscopy (see Materials and Methods) therefore enables measurements on small phase-pure single crystals as well as the selective probing of individual phases in mixed-phase nickelate crystals.

Figure 2 contrasts the distinct Raman spectra of the ML, BL, TL, and ML-TL phases. The scattering geometry including the photon polarizations are given in Porto's notation, with u indicating that no analyzer was inserted in the scattered light path, i.e., $\bar{z}(xu)z$ contains both $\bar{z}(xx)z$ and $\bar{z}(xy)z$ scattering contributions. For simplicity, the labels $\bar{z}$ and z, denoting the incident and scattered photon directions in back-scattering geometry, respectively, are omitted in the following. The x and y directions are aligned parallel to the Ni-O-Ni bond directions within the reference frame of the square-planar NiO_2 planes. The x' and y' directions are aligned at 45° to the Ni-O-Ni bonds.

Figure 2(a) shows the Raman spectrum of oxygen-stoichiometric ML La_2NiO_4, which exhibits the orthorhombic space group *Bmab* (No. 64) at room temperature. Notably, the symmetry of this material sensitively depends on the oxygen content [75]. In the present study, to enable the direct comparison between the Raman spectra of the different RP

nickelates, the sample synthesis was optimized towards full oxygen stoichiometry of the compounds (for synthesis details see Materials and Methods and Supplemental Material [68]). The spectrum in Fig. 2(a) is characterized by three prominent low-energy phonon modes between 100 and 300 cm^{-1} and an intense mode centered at 440 cm^{-1}, which involves buckling of the NiO_6 octahedra. Moreover, we observe a subtle mode around 670 cm^{-1}, which is indicative of the orthorhombic symmetry, whereas it is not present in the oxygen-excess tetragonal $I4/mmm$ (No. 139) phase of $La_2NiO_{4+\delta}$ [76].

The BL compound $La_3Ni_2O_7$ crystallizes in the orthorhombic *Amam* (No. 63) structure, although deviations from this symmetry have been reported, possibly reflecting differences in oxygen stoichiometry between samples studied in the literature [77–80]. The Raman spectrum of the BL phase is markedly distinct from that of the ML compound, with the most intense phonon mode centered at 580 cm^{-1} and an additional prominent mode at 360 cm^{-1} [Fig. 2(b)]. The former corresponds to an in-plane breathing distortion of the oxygen atoms within the NiO_2 planes, while the latter involves out-of-plane stretching of the apical oxygen atoms of the NiO_6 octahedra [46]. In addition, a broad and comparatively weak feature emerges around 1240 cm^{-1}, which was not reported in earlier Raman studies of the BL phase [40,46].

For close-to-stoichiometric oxygen contents, the TL compound $La_4Ni_3O_{10}$ realizes the monoclinic space group $P2_1/a$ (No. 14), yielding a large number of phonon modes, particularly in the low-energy range between 60 and 200 cm^{-1} [Fig. 2(c)]. The most prominent phonon mode appears near 400 cm^{-1} [41–44,47], clearly distinguishing the TL spectrum from those of the ML and BL compounds. This mode is associated with bond-stretching vibrations of basal oxygen atoms in the outer NiO_2 planes of the TL block [47]. Notably, a broad continuum of spectral weight underlies the phonon peaks and extends up to approximately 910 cm^{-1}, where it terminates in a humplike feature [green arrow in Fig. 2(c)]. Polarized Raman measurements have revealed a strong temperature dependence of this continuum, indicating gap formation associated with the intertwined CDW and SDW order in $La_4Ni_3O_{10}$ [47]. As the hump feature defines the high-energy cutoff of this continuum, it is likely associated with an electronic excitation, such as a $2\Delta_{DW}$ peak arising from short-range fluctuations of the DW that persist above the ordering temperature. Alternative interpretations cannot be fully excluded, including a multiphonon scattering origin, and a recent unpolarized Raman study proposed a bimagnon origin [81].

Figure 2(d) displays the Raman spectrum of the ML-TL polymorph. For oxygen-annealed single crystals with close-to-stoichiometric oxygen content the orthorhombic space group *Fmmm* (No. 69) was determined by high-resolution single-crystal x-ray diffraction [50]. In contrast, studies on as-grown crystals reported the orthorhombic space group *Cmmm* (No. 65) [51,52]. A key structural distinction between these two solutions is a doubling of the unit cell along the c axis and the presence of octahedral tilts in the *Fmmm* structure [Fig. 1(d)]. The Raman data shown here were acquired on an *Fmmm* crystal from the same growth batch as those reported in Ref. [50]. Remarkably, the ML-TL spectrum in Fig. 2(d) closely resembles that of the pure TL phase [Fig. 2(c)], including an intense phonon mode near 400 cm^{-1} together with a broad electronic continuum and the humplike feature around 910 cm^{-1}. Nevertheless, differences become apparent upon closer inspection of the low-energy phonon region, with at least two phonon modes around 120 and 345 cm^{-1} present in the TL phase but absent in the ML-TL polymorph, as indicated by the vertical dashed lines in Figs. 2(c) and 2(d).

Overall, Fig. 2 establishes that Raman spectroscopy provides clear, phase-specific fingerprints across the RP nickelate family, that are useful for phase identification in the context of crystal growth and sample characterization, which has proven challenging in this class of materials [82]. The close resemblance between the TL and ML-TL spectra naturally reflects the presence of TL building blocks in the polymorph, while obvious signatures associated with the ML block appear elusive in the ML-TL spectrum. To gain qualitative insight into characteristic displacement motifs associated with the ML and TL building blocks, we next examine the polarization-resolved phonons together with calculations for a high-symmetry reference structure.

B. Phonons

The *Fmmm* crystal structure of ML-TL (D_{2h} point group) gives rise to 63 Raman-active modes ($19\,A_g + 10\,B_{1g} + 17\,B_{2g} + 17\,B_{3g}$) and 68 infrared-active modes at the Γ point. The corresponding Raman tensors are presented in the Supplemental Material [68]. Figures 3(a) and 3(b) show Raman spectra of the ML-TL compound measured in four polarization configurations (xx, $x'x'$, xy, and $x'y'$) at 315 and 60 K, respectively. According to the polarization selection rules for our employed backscattering geometry with in-plane polarizations, only the A_g and B_{1g} modes are expected to be observable, with the B_{1g} modes suppressed in the xx and $x'y'$ configurations. Consistent with this expectation, phonon modes such as those near 355 and 425 cm^{-1} exhibit significantly enhanced intensity in the $x'x'$ and xy channels compared to the xx and $x'y'$ channels, respectively. Residual intensity observed in the nominally forbidden channels may arise from polarization leakage or from microscopic a/b twinning within the laser spot. By contrast, the $x'x'$ configuration allows contributions from both A_g and B_{1g} modes, and the corresponding spectrum in Fig. 3(b) exhibits the highest number of modes among the four channels, with at least 23 individual peaks discernible.

The temperature dependence of several representative phonon modes between 120 and 600 cm^{-1} in the $x'x'$ channel is displayed in Figs. 3(c) and 3(d). Upon cooling, both the low-energy modes in Fig. 3(c) and the modes near 400 cm^{-1} in Fig. 3(d) sharpen and gain intensity. In addition, a prominent cluster of modes emerges between 430 and 580 cm^{-1} and becomes increasingly pronounced upon cooling, at least down to 120 K.

The detailed temperature evolution of the phonon energy, integrated intensity, and linewidth for representative modes near 140 cm^{-1} [purple triangle in Fig. 3(c)], 400 cm^{-1} [green triangle in Fig. 3(d)], and 425 cm^{-1} [orange triangle in Fig. 3(d)] is summarized in Fig. 3(e). These parameters were extracted from Voigt-profile fits to the individual phonon peaks. Within the restricted spectral windows used for these

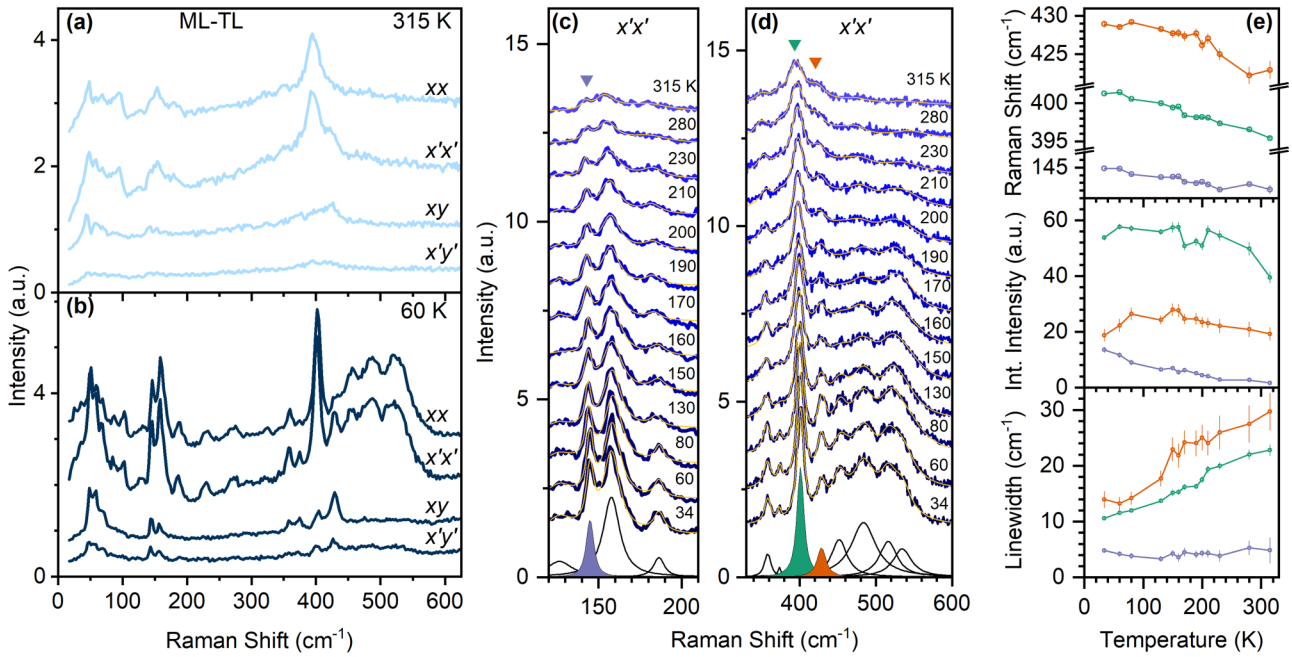


FIG. 3. Polarization-resolved Raman spectra of the phonon sector of ML-TL at (a) 315 K and (b) 60 K, acquired in xx, $x'x'$, xy, and $x'y'$ scattering configuration, respectively. For clarity, the xy and $x'x'$ spectra are offset in vertical direction by 0.5 a.u. and the xx spectra by 2 a.u. (c) Temperature dependence of selected low-energy phonon modes. Spectra are offset in vertical direction by 1 a.u. Solid yellow lines are fits of the data using Voigt profiles. Individual profiles of the 34 K fit are shown as black lines at the bottom of the panel. The phonon mode around 140 cm^{-1} is highlighted by the triangle symbol and its fitted peak profile is shaded in purple. (d) Temperature dependence of higher-energy phonon modes, with modes around 400 and 425 cm^{-1} highlighted by green and orange triangle symbols, respectively, and the corresponding peak profiles shaded in the same colors. (e) Temperature dependence of the Raman shift, integrated intensity, and linewidth of the modes evolving around 140, 400, and 425 cm^{-1} with the same color coding as in (c) and (d).

fits, the underlying electronic Raman background is nearly flat and was modeled by a constant. Asymmetric, Fano-like phonon line shapes were not observed over the investigated temperature range. The fitted individual peak profiles between 330 and 600 cm^{-1} are provided for all measured temperatures in the Supplemental Material [68]. Overall, the temperature evolution is continuous within the experimental error, without clear anomalies at specific temperatures that would indicate a structural or electronic phase transition. This behavior contrasts with the Raman spectra of the TL compound, where additional phonon modes appear below the DW transition around 140 K and subtle renormalizations of phonon self-energy parameters have been reported [47].

To obtain qualitative insight into representative atomic displacement patterns and vibrational energy scales, we perform DFPT calculations in combination with the PHONOPY package for the tetragonal $P4/mmm$ structure (see Materials and Methods). This high-symmetry reference preserves the characteristic ML-TL stacking sequence and corresponds to the experimentally established high-pressure structure of the ML-TL polymorph [50]. The c-axis lattice parameter of the $P4/mmm$ unit cell is approximately half of that of the $Fmmm$ cell and octahedral tilts are absent. A schematic comparison with the ambient-pressure $Fmmm$ structure is provided in the Supplemental Material [68].

The $P4/mmm$ unit cell (D_{4h} point group) gives rise to 18 Raman-active modes (8 A_{1g} + 9 E_g + 1 B_{1g}). A table with the calculated phonon frequencies is provided in the Supplemental Material [68]. In the c-axis backscattering geometry employed here with both photon polarizations in the ab plane, only the eight A_{1g} and one B_{1g} modes are symmetry allowed, whereas the E_g modes are forbidden. Nevertheless, a high-symmetry parent or reference structure can provide qualitative insight into phonons of a structurally related lower-symmetry phase. Specifically, in perovskites and related layered compounds it was demonstrated that upon symmetry lowering and enlargement of the translational cell, the lower-symmetry phonon manifold can contain split, zone-folded, and mixed components related to parent-phase vibrations, while characteristic local displacement motifs may remain recognizable [83–86]. For instance, it was shown for the bilayer RP compounds $Ca_3Mn_2O_7$ and $Ca_3Ti_2O_7$ that their lower-symmetry structures can be described systematically as symmetry-adapted distortions of a tetragonal $I4/mmm$ parent structure [87]. Accordingly, the calculated $P4/mmm$ eigenvectors can be used to identify representative local displacement motifs of the ML-TL lattice that potentially remain recognizable in the $Fmmm$ phonon manifold, although a one-to-one correspondence between modes of the two structures is not implied.

Figures 4(a)–4(f) show the atomic displacement patterns of representative phonon modes calculated for the $P4/mmm$ reference structure. The lowest computed mode at 48.6 cm^{-1} has E_g symmetry and involves in-plane oxygen displacements in the TL block, together with subtle displacements of apical oxygen atoms in the ML block. In addition, La atoms from both the ML and TL blocks participate in the distortion, with the largest displacements occurring on the La atoms in the outermost TL layer [Fig. 4(a)]. Nevertheless, a direct

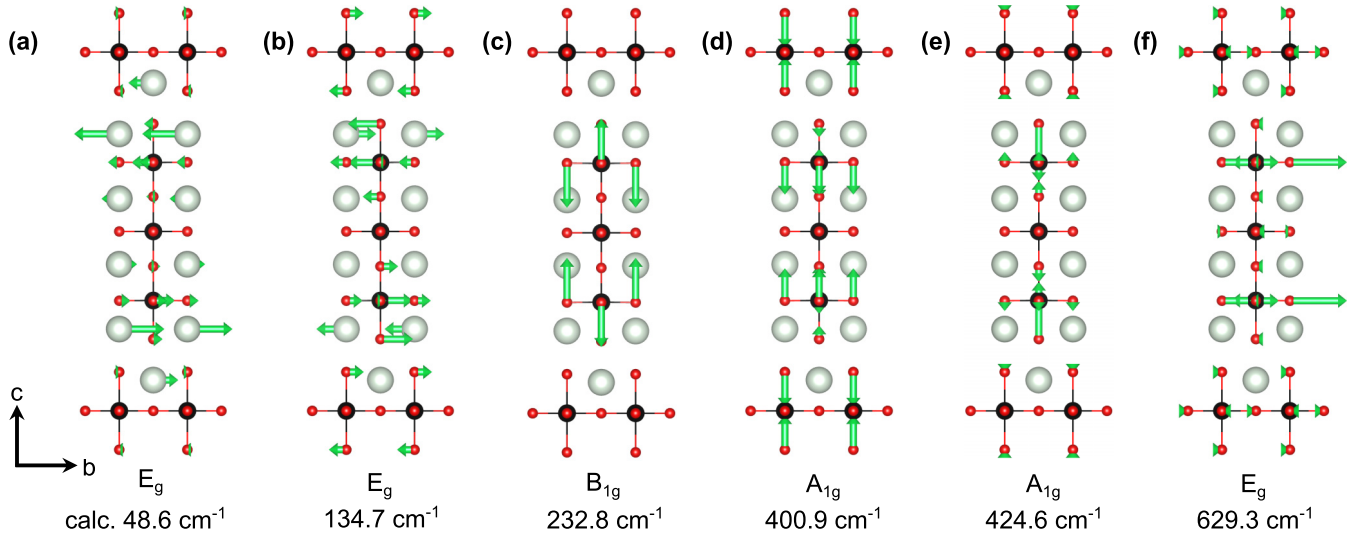


FIG. 4. (a)–(f) Atomic displacement patterns of selected phonon modes calculated for the tetragonal $P4/mmm$ high-symmetry reference structure of ML-TL. The E_g, B_{1g}, and A_{1g} mode symmetries are indicated along with the computed phonon frequencies. Green arrows display the directions and amplitudes of the atomic vibrations. For clarity, only displacements with large amplitudes are shown for each mode. The b and c directions of the $P4/mmm$ unit cell are also indicated.

correspondence between the experimentally observed phonons in Figs. 3(a) and 3(b) and the parent-structure vibration cannot be established because the $P4/mmm$ E_g mode is forbidden in the present scattering geometry. A second E_g mode, calculated at 134.7 cm^{-1}, exhibits similar in-plane oxygen motion, but without participation of the ML La atoms [Fig. 4(b)]. The only B_{1g} mode in the $P4/mmm$ structure is computed at 232.8 cm^{-1} and is characterized by out-of-plane displacements of in-plane oxygen atoms in the outer TL layers, with nearest neighbors moving antiparallel within the plane [Fig. 4(c)].

In the vicinity of 400 cm^{-1}, the calculations yield several A_{1g} modes, including a mode at 400.9 cm^{-1} that involves axial displacements of in-plane oxygen atoms against the NiO_2 planes in both the ML block and the outer TL layers [Fig. 4(d)]. Experimentally, a dominant phonon peak is observed near 400 cm^{-1} in both the ML-TL and pure TL compounds. In the latter case, however, this mode has been identified as an A_g vibration dominated by in-plane bond-stretching displacements of basal oxygen atoms in the outer NiO_2 planes [47]. These distinct displacement patterns illustrate that frequency proximity alone does not necessarily imply a common eigenvector across structurally related phases. An additional computed A_{1g} mode in the $P4/mmm$ structure at 424.6 cm^{-1} involves out-of-plane displacements of apical oxygen atoms in the outer TL layer, while distortions in the ML block are small [Fig. 4(e)]. The highest-energy computed mode at 629.3 cm^{-1} exhibits E_g symmetry and is dominated by in-plane horizontal displacements of oxygen and Ni atoms in the outer TL layer [Fig. 4(f)].

Taken together, the $P4/mmm$ reference calculations indicate that the ML unit contributes actively and in a mode-selective manner to the lattice dynamics of the ML-TL structure. A detailed mode-by-mode correspondence, however, requires future calculations for the full $Fmmm$ structure.

C. Electronic Raman response

As a next step, we examine the polarization and temperature dependence of the electronic Raman response over an extended energy range up to 2000 cm^{-1}. For the ML-TL polymorph, the hump feature at 910 cm^{-1} defines an upper energy scale beyond which the spectra in all four polarization channels are largely featureless and exhibit only a weak temperature dependence [Figs. 5(a)–5(d)]. This feature is most pronounced in the parallel polarization channels [green arrows in Figs. 5(a) and 5(b)] and is strongly suppressed in the crossed channels [Figs. 5(c) and 5(d)]. These characteristics closely resemble those reported for the corresponding 910 cm^{-1} feature in the TL compound [see Ref. [47] and green arrows in Figs. 5(e) and 5(f)], where it has been interpreted either as the $2\Delta_{DW}$ peak associated with an intertwined DW [47] or as a bimagnon excitation [81].

Remarkably, the ML-TL phase exhibits an additional distinct peaklike feature near 680 cm^{-1} at low temperatures, with a linewidth comparable to that of the 910 cm^{-1} hump. This feature is most prominent in the xy polarization channel [purple arrow in Fig. 5(c)], although weaker signatures are also visible in the other channels. No analogous feature is observed in the TL compound [Figs. 5(e)–5(h)]. Instead, the TL spectra show a pronounced suppression of spectral weight in this energy range upon cooling, extending from low energies up to the 910 cm^{-1} feature [Figs. 5(e) and 5(f)], which has been associated with the incoherent opening of the DW gap [47]. In ML-TL, a partial suppression of low-energy spectral weight is also discernible in the xy channel between 100 and 350 cm^{-1}. However, because this effect is essentially absent in the other polarization channels [Figs. 5(a), 5(b), and 5(d)], a direct analogy to the TL behavior is not straightforward.

These observations raise the question of whether the presence of the ML block can directly account for the additional 680 cm^{-1} feature unique to the ML-TL phase. To address this, we performed reference measurements on the pure ML

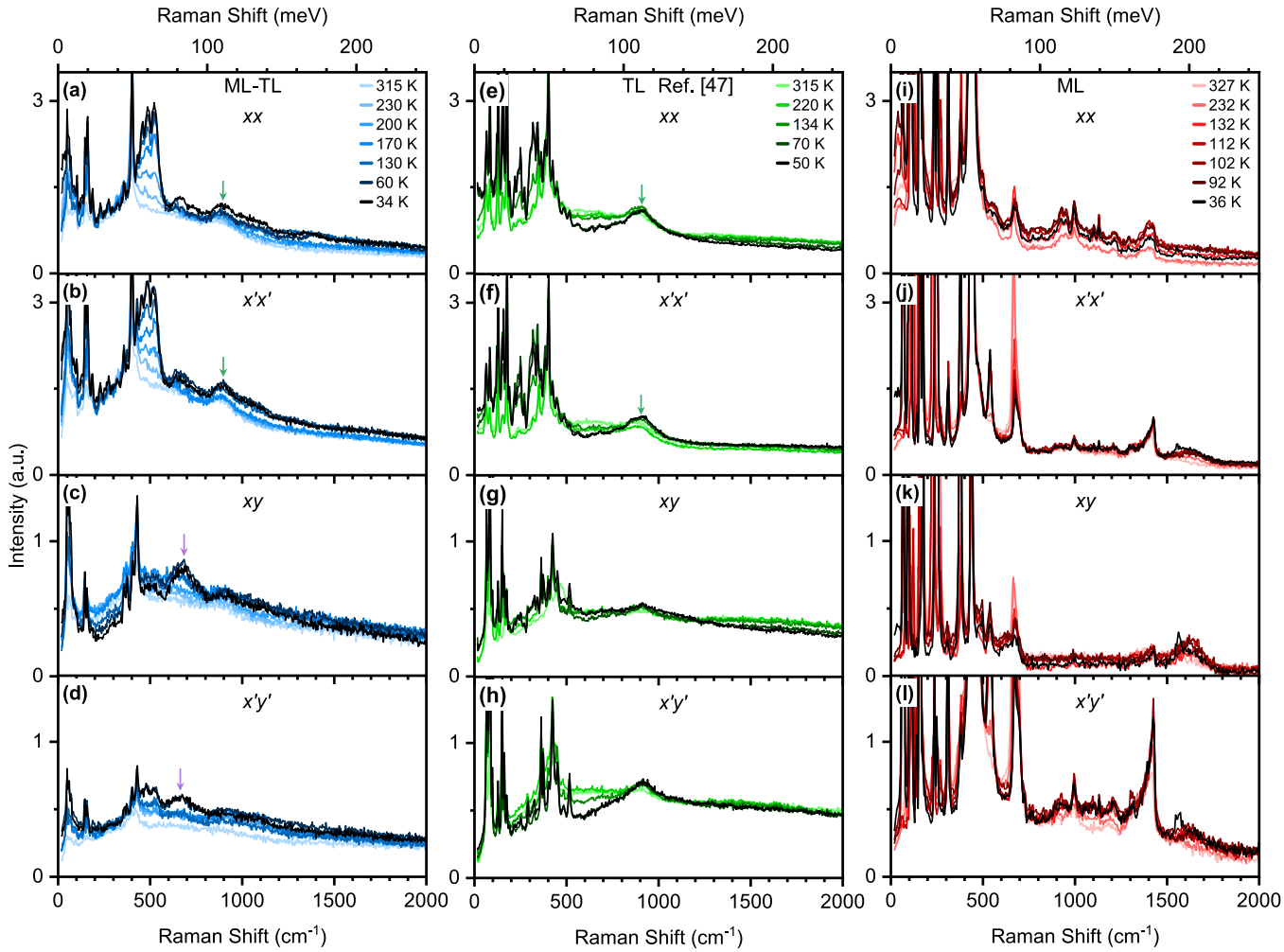


FIG. 5. Electronic Raman scattering across a wide energy range of (a)–(d) ML-TL, (e)–(h) TL, and (i)–(l) ML phases. Spectra were acquired at different temperatures (light to dark shades) and in xx, $x'x'$, xy, and $x'y'$ scattering configurations (top to bottom panel), respectively. Green arrows mark a feature around 910 cm^{-1} that occurs most prominently in the xx and $x'x'$ channels of the ML-TL and TL phases. Purple arrows highlight a feature around 680 cm^{-1} occurring most pronounced in the xy channel of ML-TL. The TL spectra in (e)–(h) are adopted from Ref. [47].

compound [Figs. 5(i)–5(l)]. While the ML spectra indeed exhibit several high-energy features, these are generally much sharper than those observed in the ML-TL and TL compounds between 500 and 910 cm^{-1}. This is also the case for a prominent feature near 680 cm^{-1} in the ML material, which is most intense in the $x'x'$ and $x'y'$ polarization channels and can be assigned to a phonon mode. Moreover, in contrast to the ML-TL spectra, this mode in the ML compound shows a significant reduction in spectral weight upon cooling from 327 to 36 K [Fig. 5(j)], consistent with a phononic origin and with its relation to the orthorhombic-to-tetragonal structural phase transition of the ML compound at low temperatures [76]. Several of the higher-energy features in ML are multiphonon peaks and the broad feature around 1700 cm^{-1} likely corresponds to a bimagnon [88].

Nevertheless, an electronic Raman feature reminiscent of the 680 cm^{-1} peak in ML-TL has been reported in the BL compound below 150 K, where it was attributed to SDW formation [40]. Notably, in the BL compound the characteristic 650 cm^{-1} feature emerges exclusively in the xy channel, whereas in our ML-TL spectra it persists in multiple polarization channels, albeit with reduced intensity. Furthermore, BL exhibits a second SDW-related feature appearing only in the $x'y'$ channel near 370 cm^{-1}. In ML-TL, spectral weight gain at low temperatures is also observed in the $x'y'$ channel around 500 cm^{-1}, which however might be associated with increasing intensity of closely spaced phonon modes in this energy range.

Overall, the low-temperature evolution of the integrated spectral weight in the 430–600 cm^{-1} range is less clearly monotonic than at higher temperatures, leaving open the possibility of an additional electronic contribution. At the same time, the pronounced internal peak structure (see detailed fits with individual peak profiles in the Supplemental Material) indicates that a substantial phononic component remains present. In contrast, the 680 cm^{-1} feature shows a qualitatively different temperature dependence, exhibiting a pronounced intensity enhancement with an onset between 170 and 200 K. Therefore, the 680 cm^{-1} feature is attributed to electronic Raman scattering likely associated with DW

formation. Taken together, since none of the low-temperature emergent features can be directly traced to an origin in the isolated ML block, the electronic Raman response of the ML-TL polymorph cannot be understood as a simple superposition of its ML and TL constituents, but instead reflects a distinct electronic structure intrinsic to the ML-TL phase.

IV. DISCUSSION

Our comparative Raman study reveals a nuanced interplay between lattice dynamics and electronic excitations in the ML-TL polymorph, highlighting both similarities to and important departures from the behavior of the pure TL and BL compounds. At room temperature, the phononic Raman response of the ML-TL phase closely resembles that of the pure TL compound. However, the $P4/mmm$ reference calculations reveal representative displacement patterns involving atoms in both the ML and TL blocks, showing that the ML-TL lattice supports Raman-active vibrational motifs involving both structural constituents. Specifically, while the TL block remains a dominant contributor to the lattice dynamics, the ML block is clearly not only a passive structural spacer. Instead, it hybridizes with TL-derived vibrations and actively shapes the phonon spectrum of the ML-TL polymorph.

Beyond similarities and subtle differences to the TL spectra at room temperature, unique characteristics of the phononic Raman response of the ML-TL phase emerge upon cooling. In particular, a pronounced cluster of modes emerges between 430 and 600 cm^{-1}, most prominently in the xx and $x'x'$ polarization channels. Its pronounced internal peak structure demonstrates a substantial phononic contribution, while an additional or mixed contribution from an electronic excitation cannot be separated unambiguously in the present data.

In contrast to the continuous temperature evolution of the well-resolved lower-energy phonons, the electronic Raman scattering shows qualitatively new features at low temperatures. Specifically, a broad feature develops near 680 cm^{-1} that has no direct analog in the TL compound and also differs from the polarization selection rules of the SDW feature reported for the BL phase [40]. The distinctive symmetry-dependent redistribution of spectral weight at low temperatures indicates that a simple transfer of the BL SDW scenario to the ML-TL phase is insufficient. Furthermore, the vanishing of spectral weight associated with the DW gap opening in the pure TL compound [47] is absent or superposed by the emergence of the 680 cm^{-1} feature in ML-TL. Nevertheless, the feature near 910 cm^{-1} attributed to short-range CDW fluctuations in pure TL [47] occurs closely similar in ML-TL across the different polarization channels, indicating comparable CDW correlations in the TL block of ML-TL.

These findings suggest that the ML-TL polymorph does not simply inherit the DW physics of the TL or the BL compound, but instead realizes an at least partially distinct correlated electronic state. This conclusion is consistent with recent theoretical work predicting that the periodic insertion of ML blocks leads to a more complex electronic structure than in the pure TL phase, including additional Fermi surface sheets and enhanced correlations [62,67]. The ML blocks therefore not only modify the lattice dynamics but also qualitatively alter the low-energy electronic excitations probed by Raman scattering.

V. CONCLUSION

In summary, our study compared the unique Raman spectroscopic fingerprints of the RP family members ML La_2NiO_4, BL $La_3Ni_2O_7$, TL $La_4Ni_3O_{10}$, and the polymorph ML-TL $La_3Ni_2O_7$, providing clear benchmarks for phase identification and characterization studies. A central result is that, although the room-temperature Raman spectra of ML-TL and TL appear closely similar, pronounced differences emerge at low temperatures, particularly affecting the polarization-resolved electronic Raman response. We attribute these contrasts to subtle but important differences in the underlying electronic structures of the two materials, driven by self-doping and quantum-confinement effects from the ML unit in the ML-TL crystal structure. Understanding how these differences relate to superconductivity, in particular to the possibly reduced T_c of ML-TL [53] compared to TL and BL, will be an important direction for future work.

ACKNOWLEDGMENTS

We thank A. Greco, M. J. Graf von Westarp, A. von Ungern-Sternberg Schwark, and S. Hameed for insightful discussions. X.W. is supported by the National Key R&D Program of China (Grant No. 2023YFA1407300) and the National Natural Science Foundation of China (Grants No. 12574151, No. 12447103, and No. 12447101).

DATA AVAILABILITY

There are no publicly available research data or software supporting this manuscript. Requests for further information or data should be sent to the authors.

[1] M. R. Norman, Materials design for new superconductors, Rep. Prog. Phys. **79**, 074502 (2016).

[2] J. Acrivos, M. Lei, C. Jiang, H. Nguyen, P. Metcalf, and J. Honig, Paramagnetism, antiferromagnetism, and superconductivity in La_2NiO_4, J. Solid State Chem. **111**, 343 (1994).

[3] V. Sachan, D. J. Buttrey, J. M. Tranquada, J. E. Lorenzo, and G. Shirane, Charge and spin ordering in $La_{2-x}Sr_xNiO_{4.00}$ with $x = 0.135$ and 0.20, Phys. Rev. B **51**, 12742 (1995).

[4] J. M. Tranquada, Cuprate superconductors as viewed through a striped lens, Adv. Phys. **69**, 437 (2020).

[5] B. Keimer, S. A. Kivelson, M. R. Norman, S. Uchida, and J. Zaanen, From quantum matter to high-temperature superconductivity in copper oxides, Nature (London) **518**, 179 (2015).

[6] D. J. Scalapino, A common thread: The pairing interaction for unconventional superconductors, Rev. Mod. Phys. **84**, 1383 (2012).

[7] Y. Ji, X. Wang, X. Li, W. Tang, X. Li, X. Wang, F. Li, L. Li, and Q. Zhou, Unveiling a novel insulator-to-metal transition in $La_2NiO_{4+\delta}$: Challenging high-temperature superconductivity

claimed for single-layer lanthanum nickelates, Chin. Phys. Lett. **41**, 097402 (2024).

[8] M. Uchida, K. Ishizaka, P. Hansmann, Y. Kaneko, Y. Ishida, X. Yang, R. Kumai, A. Toschi, Y. Onose, R. Arita, K. Held, O. K. Andersen, S. Shin, and Y. Tokura, Pseudogap of metallic layered nickelate $R_{2-x}Sr_xNiO_4$ (R = Nd, Eu) crystals measured using angle-resolved photoemission spectroscopy, Phys. Rev. Lett. **106**, 027001 (2011).

[9] S. Middey, J. Chakhalian, P. Mahadevan, J. Freeland, A. Millis, and D. Sarma, Physics of ultrathin films and heterostructures of rare-earth nickelates, Annu. Rev. Mater. Res. **46**, 305 (2016).

[10] J. Chaloupka and G. Khaliullin, Orbital order and possible superconductivity in $LaNiO_3/LaMO_3$ superlattices, Phys. Rev. Lett. **100**, 016404 (2008).

[11] P. Hansmann, X. Yang, A. Toschi, G. Khaliullin, O. K. Andersen, and K. Held, Turning a nickelate Fermi surface into a cupratelike one through heterostructuring, Phys. Rev. Lett. **103**, 016401 (2009).

[12] D. Li, K. Lee, B. Y. Wang, M. Osada, S. Crossley, H. R. Lee, Y. Cui, Y. Hikita, and H. Y. Hwang, Superconductivity in an infinite-layer nickelate, Nature (London) **572**, 624 (2019).

[13] P. Puphal, T. Schäfer, B. Keimer, and M. Hepting, Superconductivity in infinite-layer and Ruddlesden–Popper nickelates, Nat. Rev. Phys. **8**, 70 (2026).

[14] B. Y. Wang, K. Lee, and B. H. Goodge, Experimental progress in superconducting nickelates, Annu. Rev. Condens. Matter Phys. **15**, 305 (2024).

[15] V. I. Anisimov, D. Bukhvalov, and T. M. Rice, Electronic structure of possible nickelate analogs to the cuprates, Phys. Rev. B **59**, 7901 (1999).

[16] G. A. Pan, D. F. Segedin, H. LaBollita, Q. Song, E. M. Nica, B. H. Goodge, A. T. Pierce, S. Doyle, S. Novakov, D. C. Carrizales, A. T. N'Diaye, P. Shafer, H. Paik, J. T. Heron, J. A. Mason, A. Yacoby, L. F. Kourkoutis, O. Erten, C. M. Brooks, A. S. Botana, *et al.*, Superconductivity in a quintuple-layer square-planar nickelate, Nat. Mater. **21**, 160 (2022).

[17] H. Sun, M. Huo, X. Hu, J. Li, Z. Liu, Y. Han, L. Tang, Z. Mao, P. Yang, B. Wang, J. Cheng, D.-X. Yao, G.-M. Zhang, and M. Wang, Signatures of superconductivity near 80 K in a nickelate under high pressure, Nature (London) **621**, 493 (2023).

[18] E. K. Ko, Y. Yu, Y. Liu, L. Bhatt, J. Li, V. Thampy, C.-T. Kuo, B. Y. Wang, Y. Lee, K. Lee, J.-S. Lee, B. H. Goodge, D. A. Muller, and H. Y. Hwang, Signatures of ambient pressure superconductivity in thin film $La_3Ni_2O_7$, Nature (London) **638**, 935 (2025).

[19] G. Zhou, W. Lv, H. Wang, Z. Nie, Y. Chen, Y. Li, H. Huang, W. Chen, Y. Sun, Q.-K. Xue, and Z. Chen, Ambient-pressure superconductivity onset above 40 K in $(La, Pr)_3Ni_2O_7$ films, Nature (London) **640**, 641 (2025).

[20] M. Hepting, Nickelates join the club of high-temperature superconductors, Nature (London) **621**, 475 (2023).

[21] M. Greenblatt, Ruddlesden-Popper $Ln_{n+1}Ni_nO_{3n+1}$ nickelates: Structure and properties, Curr. Opin. Solid State Mater. Sci. **2**, 174 (1997).

[22] Y. Zhu, D. Peng, E. Zhang, B. Pan, X. Chen, L. Chen, H. Ren, F. Liu, Y. Hao, N. Li, Z. Xing, F. Lan, J. Han, J. Wang, D. Jia, H. Wo, Y. Gu, Y. Gu, L. Ji, W. Wang, *et al.*, Superconductivity in pressurized trilayer $La_4Ni_3O_{10-\delta}$ single crystals, Nature (London) **631**, 531 (2024).

[23] M. Zhang, C. Pei, D. Peng, X. Du, W. Hu, Y. Cao, Q. Wang, J. Wu, Y. Li, H. Liu, C. Wen, J. Song, Y. Zhao, C. Li, W. Cao, S. Zhu, Q. Zhang, N. Yu, P. Cheng, L. Zhang, *et al.*, Superconductivity in trilayer nickelate $La_4Ni_3O_{10}$ under pressure, Phys. Rev. X **15**, 021005 (2025).

[24] A. Iyo, Y. Tanaka, H. Kito, Y. Kodama, P. M. Shirage, D. D. Shivagan, H. Matsuhata, K. Tokiwa, and T. Watanabe, T_c vs n relationship for multilayered high-T_c superconductors, J. Phys. Soc. Jpn. **76**, 094711 (2007).

[25] M. Wang, H.-H. Wen, T. Wu, D.-X. Yao, and T. Xiang, Normal and superconducting properties of $La_3Ni_2O_7$, Chin. Phys. Lett. **41**, 077402 (2024).

[26] C. Lu, Z. Pan, F. Yang, and C. Wu, Superconductivity in $La_4Ni_3O_{10}$ under pressure, Phys. Rev. B **111**, 134515 (2025).

[27] J. Huang and T. Zhou, Interlayer pairing-induced partially gapped Fermi surface in trilayer $La_4Ni_3O_{10}$ superconductors, Phys. Rev. B **110**, L060506 (2024).

[28] G. Khaliullin and J. Chaloupka, Orbital order and superconductivity in bilayer nickelate compounds, Phys. Rev. B **113**, L041115 (2026).

[29] M. Bejas, X. Wu, D. Chakraborty, A. P. Schnyder, and A. Greco, Out-of-plane bond-order phase, superconductivity, and their competition in the t-$J_\parallel$–$J_\perp$ model: Possible implications for bilayer nickelates, Phys. Rev. B **111**, 144514 (2025).

[30] H. Sakakibara, M. Ochi, H. Nagata, Y. Ueki, H. Sakurai, R. Matsumoto, K. Terashima, K. Hirose, H. Ohta, M. Kato, Y. Takano, and K. Kuroki, Theoretical analysis on the possibility of superconductivity in the trilayer Ruddlesden-Popper nickelate $La_4Ni_3O_{10}$ under pressure and its experimental examination: Comparison with $La_3Ni_2O_7$, Phys. Rev. B **109**, 144511 (2024).

[31] R. M. Fernandes, A. I. Coldea, H. Ding, I. R. Fisher, P. J. Hirschfeld, and G. Kotliar, Iron pnictides and chalcogenides: A new paradigm for superconductivity, Nature (London) **601**, 35 (2022).

[32] J. Zhang, D. Phelan, A. S. Botana, Y.-S. Chen, H. Zheng, M. Krogstad, S. G. Wang, Y. Qiu, J. A. Rodriguez-Rivera, R. Osborn, S. Rosenkranz, M. R. Norman, and J. F. Mitchell, Intertwined density waves in a metallic nickelate, Nat. Commun. **11**, 6003 (2020).

[33] Z. Liu, H. Sun, M. Huo, X. Ma, Y. Ji, E. Yi, L. Li, H. Liu, J. Yu, Z. Zhang, Z. Chen, F. Liang, H. Dong, H. Guo, D. Zhong, B. Shen, S. Li, and M. Wang, Evidence for charge and spin density waves in single crystals of $La_3Ni_2O_7$ and $La_3Ni_2O_6$, Sci. China Phys. Mech. Astron. **66**, 217411 (2023).

[34] H. Li, X. Zhou, T. Nummy, J. Zhang, V. Pardo, W. E. Pickett, J. F. Mitchell, and D. S. Dessau, Fermiology and electron dynamics of trilayer nickelate $La_4Ni_3O_{10}$, Nat. Commun. **8**, 704 (2017).

[35] Z. Liu, M. Huo, J. Li, Q. Li, Y. Liu, Y. Dai, X. Zhou, J. Hao, Y. Lu, M. Wang, and H.-H. Wen, Electronic correlations and partial gap in the bilayer nickelate $La_3Ni_2O_7$, Nat. Commun. **15**, 7570 (2024).

[36] S. Xu, C.-Q. Chen, M. Huo, D. Hu, H. Wang, Q. Wu, R. Li, D. Wu, M. Wang, D.-X. Yao, T. Dong, and N. Wang, Origin of the density wave instability in trilayer nickelate $La_4Ni_3O_{10}$ revealed by optical and ultrafast spectroscopy, Phys. Rev. B **111**, 075140 (2025).

[37] K. Chen, X. Liu, J. Jiao, M. Zou, C. Jiang, X. Li, Y. Luo, Q. Wu, N. Zhang, Y. Guo, and L. Shu, Evidence of spin density waves in $La_3Ni_2O_{7-\delta}$, Phys. Rev. Lett. **132**, 256503 (2024).

[38] R. Khasanov, T. J. Hicken, D. J. Gawryluk, V. Sazgari, I. Plokhikh, L. P. Sorel, M. Bartkowiak, S. Bötzel, F. Lechermann, I. M. Eremin, H. Luetkens, and Z. Guguchia, Pressure-enhanced splitting of density wave transitions in $La_3Ni_2O_7$, Nat. Phys. **21**, 430 (2025).

[39] M. Kakoi, T. Oi, Y. Ohshita, M. Yashima, K. Kuroki, T. Kato, H. Takahashi, S. Ishiwata, Y. Adachi, N. Hatada, T. Uda, and H. Mukuda, Multiband metallic ground state in multilayered nickelates $La_3Ni_2O_7$ and $La_4Ni_3O_{10}$ probed by $^{139}La-$NMR at ambient pressure, J. Phys. Soc. Jpn. **93**, 053702 (2024).

[40] G. He, J. Shen, S. Xie, H. Zhang, M. Huo, J. Shu, D. Hu, X. Zhou, Y. Zhang, L. Qin, L. Qiao, H. Liu, C. Hu, X. Dong, D. Wang, J. Liu, W. Hu, J. Yuan, Y. Yan, Z. Qi, *et al.*, Anisotropic electronic correlations in the spin density wave state of $La_3Ni_2O_7$, Nat. Commun. **17**, 6272 (2026).

[41] Y. Li, Y. Cao, L. Liu, P. Peng, H. Lin, C. Pei, M. Zhang, H. Wu, X. Du, W. Zhao, K. Zhai, X. Zhang, J. Zhao, M. Lin, P. Tan, Y. Qi, G. Li, H. Guo, L. Yang, and L. Yang, Distinct ultrafast dynamics of bilayer and trilayer nickelate superconductors regarding the density-wave-like transitions, Sci. Bull. **70**, 180 (2025).

[42] S. Deswal, D. Kumar, D. Rout, S. Singh, and P. Kumar, Dynamics of electron–electron correlation and electron–phonon coupled phase progression in trilayer nickelate $La_4Ni_3O_{10}$, Appl. Phys. Lett. **127**, 071903 (2025).

[43] S. Ramakrishnan, Y. Gao, V. Olevano, E. Pachoud, A. Hadj-Azzem, G. Garbarino, M. d'Astuto, O. Perez, A. Pautrat, D. Valenti, M. Quénot, S. Pairis, D. Chernyshov, L. Noohinejad, C. Paulmann, J. Bulled, A. Bosak, S. van Smaalen, P. Toulemonde, M.-A. Méasson, *et al.*, Tracing the horizon of tetragonal-to-monoclinic distortion in pressurized trilayer nickelate $La_4Ni_3O_{10}$, Commun. Mater. **7**, 248 (2026).

[44] D.-H. Gim, C. H. Park, and K. H. Kim, Orbital-selective quasiparticle depletion across the density wave transition in trilayer nickelate $La_4Ni_3O_{10}$, Phys. Rev. Lett. **135**, 136505 (2025).

[45] S. Deswal, D. Rout, N. Jana, K. Pal, S. Singh, and P. Kumar, Interplay of phonons, intertwined density waves, and induced spin density wave in trilayer nickelates $Pr_{4-x}La_xNi_3O_{10}$, Phys. Rev. B **112**, 235151 (2025).

[46] H. Zhang, J. Zhang, M. Huo, J. Chen, D. Hu, D.-X. Yao, H. Sun, K. Cao, and M. Wang, Identifying the structure of $La_3Ni_2O_7$ in the pressurized superconducting state, arXiv:2511.15265v3.

[47] A. Suthar, V. Sundaramurthy, M. Bejas, C. Le, P. Puphal, P. Sosa-Lizama, A. Schulz, J. Nuss, M. Isobe, P. A. van Aken, Y. E. Suyolcu, M. Minola, A. P. Schnyder, X. Wu, B. Keimer, G. Khaliullin, A. Greco, and M. Hepting, Multiorbital character of the density wave in trilayer nickelate superconductors, Phys. Rev. B **114**, 045132 (2026).

[48] F. Li, N. Guo, Q. Zheng, Y. Shen, S. Wang, Q. Cui, C. Liu, S. Wang, X. Tao, G.-M. Zhang, and J. Zhang, Design and synthesis of three-dimensional hybrid Ruddlesden-Popper nickelate single crystals, Phys. Rev. Mater. **8**, 053401 (2024).

[49] M. Shi, D. Peng, K. Fan, Z. Xing, S. Yang, Y. Wang, H. Li, R. Wu, M. Du, B. Ge, Z. Zeng, Q. Zeng, J. Ying, T. Wu, and X. Chen, Pressure induced superconductivity in hybrid Ruddlesden-Popper $La_5Ni_3O_{11}$ single crystals, Nat. Phys. **21**, 1780 (2025).

[50] P. Puphal, P. Reiss, N. Enderlein, Y.-M. Wu, G. Khaliullin, V. Sundaramurthy, T. Priessnitz, M. Knauft, A. Suthar, L. Richter, M. Isobe, P. A. van Aken, H. Takagi, B. Keimer, Y. E. Suyolcu, B. Wehinger, P. Hansmann, and M. Hepting, Unconventional crystal structure of the high-pressure superconductor $La_3Ni_2O_7$, Phys. Rev. Lett. **133**, 146002 (2024).

[51] X. Chen, J. Zhang, A. S. Thind, S. Sharma, H. LaBollita, G. Peterson, H. Zheng, D. P. Phelan, A. S. Botana, R. F. Klie, and J. F. Mitchell, Polymorphism in the Ruddlesden–Popper nickelate $La_3Ni_2O_7$: Discovery of a hidden phase with distinctive layer stacking, J. Am. Chem. Soc. **146**, 3640 (2024).

[52] H. Wang, L. Chen, A. Rutherford, H. Zhou, and W. Xie, Long-range structural order in a hidden phase of Ruddlesden–Popper bilayer nickelate $La_3Ni_2O_7$, Inorg. Chem. **63**, 5020 (2024).

[53] C. Huang, J. Li, X. Huang, H. Zhang, D. Hu, M. Huo, X. Chen, Z. Chen, H. Sun, and M. Wang, Superconductivity in monolayer-trilayer phase of $La_3Ni_2O_7$ under high pressure, Phys. Rev. X **16**, 031072 (2026).

[54] C. C. Au-Yeung, X. Chen, S. Smit, M. Bluschke, V. Zimmermann, M. Michiardi, P. C. Moen, J. Kraan, C. S. B. Pang, C. T. Suen, S. Zhdanovich, M. Zonno, S. Gorovikov, Y. Liu, P. Dosanjh, G. Levy, I. S. Elfimov, M. Berciu, G. A. Sawatzky, J. F. Mitchell, *et al.*, Oxygen-centred planar orbitals in the electronic structure and spin-density-wave reconstruction of multilayer nickelates, Nat. Phys. **22**, 1087 (2026).

[55] Z. Luo, B. Lv, M. Wang, W. Wú, and D.-X. Yao, High-T_C superconductivity in $La_3Ni_2O_7$ based on the bilayer two-orbital t-J model, npj Quantum Mater. **9**, 61 (2024).

[56] C. Lu, Z. Pan, F. Yang, and C. Wu, Interlayer-coupling-driven high-temperature superconductivity in $La_3Ni_2O_7$ under pressure, Phys. Rev. Lett. **132**, 146002 (2024).

[57] S. Ryee, N. Witt, and T. O. Wehling, Quenched pair breaking by interlayer correlations as a key to superconductivity in $La_3Ni_2O_7$, Phys. Rev. Lett. **133**, 096002 (2024).

[58] K.-Y. Jiang, Y.-H. Cao, Q.-G. Yang, H.-Y. Lu, and Q.-H. Wang, Theory of pressure dependence of superconductivity in bilayer nickelate $La_3Ni_2O_7$, Phys. Rev. Lett. **134**, 076001 (2025).

[59] S. Abadi, K.-J. Xu, E. G. Lomeli, P. Puphal, M. Isobe, Y. Zhong, A. V. Fedorov, S.-K. Mo, M. Hashimoto, D.-H. Lu, B. Moritz, B. Keimer, T. P. Devereaux, M. Hepting, and Z.-X. Shen, Electronic structure of the alternating monolayer-trilayer phase of $La_3Ni_2O_7$, Phys. Rev. Lett. **134**, 126001 (2025).

[60] M. Uchida, K. Ishizaka, P. Hansmann, X. Yang, M. Sakano, J. Miyawaki, R. Arita, Y. Kaneko, Y. Takata, M. Oura, A. Toschi, K. Held, A. Chainani, O. K. Andersen, S. Shin, and Y. Tokura, Orbital characters of three-dimensional Fermi surfaces in $Eu_{2-x}Sr_xNiO_4$ as probed by soft-x-ray angle-resolved photoemission spectroscopy, Phys. Rev. B **84**, 241109 (2011).

[61] J. Yang, H. Sun, X. Hu, Y. Xie, T. Miao, H. Luo, H. Chen, B. Liang, W. Zhu, G. Qu, C.-Q. Chen, M. Huo, Y. Huang, S. Zhang, F. Zhang, F. Yang, Z. Wang, Q. Peng, H. Mao, G. Liu, *et al.*, Orbital-dependent electron correlation in double-layer nickelate $La_3Ni_2O_7$, Nat. Commun. **15**, 4373 (2024).

[62] H. LaBollita, S. Bag, J. Kapeghian, and A. S. Botana, Electronic correlations, layer distinction, and electron doping in the alternating single-layer–trilayer $La_3Ni_2O_7$ polymorph, Phys. Rev. B **110**, 155145 (2024).

[63] Y. Zhang, L.-F. Lin, A. Moreo, T. A. Maier, and E. Dagotto, Electronic structure, self-doping, and superconducting instability in the alternating single-layer trilayer

stacking nickelates $La_3Ni_2O_7$, Phys. Rev. B **110**, L060510 (2024).

[64] Y. Liu, Z. Liu, D. Zhang, J.-M. Liu, and Y. Yang, Magnetic and electronic properties in Ruddlesden–Popper lanthanum nickelates from first-principles calculations, J. Phys. Chem. C **129**, 19074 (2025).

[65] Z. Ouyang, J.-M. Wang, R.-Q. He, and Z.-Y. Lu, DFT + DMFT study of correlated electronic structure in the monolayer-trilayer phase of $La_3Ni_2O_7$, Phys. Rev. B **111**, 125111 (2025).

[66] B. Samanta and A. B. Georgescu, In-plane Ni–O–Ni bond angles as structural fingerprints of superconductivity in layered nickelates: Effects of pressure, strain, layering, and correlations, Phys. Rev. Mater. **9**, 114801 (2025).

[67] F. Lechermann, S. Bötzel, and I. M. Eremin, Electronic instability, layer selectivity, and Fermi arcs in $La_3Ni_2O_7$, Phys. Rev. Mater. **8**, 074802 (2024).

[68] See Supplemental Material at http://link.aps.org/supplemental/10.1103/m2js-yzky for additional information on sample synthesis, characterization, phonon frequency calculations and Raman measurements, which includes Refs. [47,50,89].

[69] G. Kresse and J. Furthmüller, Efficient iterative schemes for *ab initio* total-energy calculations using a plane-wave basis set, Phys. Rev. B **54**, 11169 (1996).

[70] J. P. Perdew, K. Burke, and M. Ernzerhof, Generalized gradient approximation made simple, Phys. Rev. Lett. **77**, 3865 (1996).

[71] G. Kresse and D. Joubert, From ultrasoft pseudopotentials to the projector augmented-wave method, Phys. Rev. B **59**, 1758 (1999).

[72] S. Baroni, P. Giannozzi, and A. Testa, Green's-function approach to linear response in solids, Phys. Rev. Lett. **58**, 1861 (1987).

[73] A. Togo, F. Oba, and I. Tanaka, First-principles calculations of the ferroelastic transition between rutile-type and $CaCl_2$-type SiO_2, at high pressures, Phys. Rev. B **78**, 134106 (2008).

[74] A. Togo and I. Tanaka, First principles phonon calculations in materials science, Scr. Mater. **108**, 1 (2015).

[75] N. Poirot, P. Simon, P. Odier, and J. Bassat, Magnetic resonance in oxygen-doped $La_2NiO_{4+\delta}$, Eur. Phys. J. B **2**, 469 (1998).

[76] A. Riaz, A. Stangl, M. Burriel, and M. Mermoux, *In situ* observation of phase transitions in $La_2NiO_{4+\delta}$ bulk and thin film samples via Raman spectroscopy, Acta Mater. **301**, 121570 (2025).

[77] Z. Zhang, M. Greenblatt, and J. B. Goodenough, Synthesis, structure, and properties of the layered perovskite $La_3Ni_2O_7$, J. Solid State Chem. **108**, 402 (1994).

[78] Z. Dong, M. Huo, J. Li, J. Li, P. Li, H. Sun, L. Gu, Y. Lu, M. Wang, Y. Wang, and Z. Chen, Visualization of oxygen vacancies and self-doped ligand holes in $La_3Ni_2O_{7-\delta}$, Nature (London) **630**, 847 (2024).

[79] X. Chen, N. Wang, Q. Zhang, B. Wang, G. Wang, B. Wang, J. Cheng, and L. Gu, Interlayer switching of NiO_6 octahedra tilt via interstitial oxygen in $La_{n+1}Ni_nO_{3n+1}$ ($n = 1, 2, 3$), Adv. Mater. **37**, e04238 (2025).

[80] L. Wang, Y. Li, S.-Y. Xie, F. Liu, H. Sun, C. Huang, Y. Gao, T. Nakagawa, B. Fu, B. Dong, Z. Cao, R. Yu, S. I. Kawaguchi, H. Kadobayashi, M. Wang, C. Jin, H.-k. Mao, and H. Liu, Structure responsible for the superconducting state in $La_3Ni_2O_7$ at high-pressure and low-temperature conditions, J. Am. Chem. Soc. **146**, 7506 (2024).

[81] S. Zhang, H. Zhang, Z. Dong, J. Li, Q. Xiao, M. Huo, H.-Y. Huang, D.-J. Huang, Y. Wang, Y. Lu, Z. Chen, M. Wang, and Y. Peng, Distinct orbital contributions to electronic and magnetic structures in $La_4Ni_3O_{10}$, Phys. Rev. Res. **8**, 023119 (2026).

[82] Y. Zhou, J. Guo, S. Cai, H. Sun, C. Li, J. Zhao, P. Wang, J. Han, X. Chen, Y. Chen, Q. Wu, Y. Ding, T. Xiang, H.-k. Mao, and L. Sun, Investigations of key issues on the reproducibility of high-T_c superconductivity emerging from compressed $La_3Ni_2O_7$, Matter Radiat. Extremes **10**, 027801 (2025).

[83] C. Toulouse, D. Amoroso, C. Xin, P. Veber, M. C. Hatnean, G. Balakrishnan, M. Maglione, P. Ghosez, J. Kreisel, and M. Guennou, Lattice dynamics and Raman spectrum of $BaZrO_3$ single crystals, Phys. Rev. B **100**, 134102 (2019).

[84] C. Toulouse, D. Amoroso, R. Oliva, C. Xin, P. Bouvier, P. Fertey, P. Veber, M. Maglione, P. Ghosez, J. Kreisel, and M. Guennou, Stability of the tetragonal phase of $BaZrO_3$ under high pressure, Phys. Rev. B **106**, 064105 (2022).

[85] R. A. Evarestov, E. Blokhin, D. Gryaznov, E. A. Kotomin, and J. Maier, Phonon calculations in cubic and tetragonal phases of $SrTiO_3$: A comparative LCAO and plane-wave study, Phys. Rev. B **83**, 134108 (2011).

[86] A. P. Ayala, I. Guedes, E. N. Silva, M. S. Augsburger, M. del C. Viola, and J. C. Pedregosa, Raman investigation of A_2CoBO_6 (A = Sr and Ca, B = Te and W) double perovskites, J. Appl. Phys. **101**, 123511 (2007).

[87] A. B. Harris, Symmetry analysis for the Ruddlesden-Popper systems $Ca_3Mn_2O_7$ and $Ca_3Ti_2O_7$, Phys. Rev. B **84**, 064116 (2011).

[88] S. Sugai, N. Kitamori, S. Hosoya, and K. Yamada, Separation of spin and charge densities in $La_2NiO_{4+\delta}$, J. Phys. Soc. Jpn. **67**, 2992 (1998).

[89] P. Puphal, V. Sundaramurthy, V. Zimmermann, K. Küster, U. Starke, M. Isobe, B. Keimer, and M. Hepting, Phase formation in hole- and electron-doped rare-earth nickelate single crystals, APL Mater. **11**, 081107 (2023).